sciendo

TRANSACTIONS ON AEROSPACE RESEARCH
eISSN 2545-2835, VOL. 276, NO. 3/2024, 86-100
DOI: 10.2478/tar-2024-0018

Łukasiewicz
Institute
of Aviation

# TEST SECTION DESIGN FOR MEASURING THE DRAG COEFFICIENT OF A SUBORBITAL ROCKET MODEL AT MA 2.45

**Filip Wasilczuk*** 0000-0002-8658-5622
**Marcin Kurowski** 0000-0002-5260-1356
**Paweł Flaszyński** 0000-0002-4210-804X
Institute of Fluid-Flow Machinery, Polish Academy of Sciences, Fiszera 14, 80-231 Gdansk, Poland

## ABSTRACT

This study investigates the drag coefficient of three models of suborbital rockets with different nosecones. A test section allowing for force measurement of a 1:50 scale rocket model was designed with the aid of numerical simulations. The velocity obtained in the wind tunnel corresponds with a Mach number of 2.45. RANS simulations were used in verifying operating parameters, as well as testing the support configurations for connecting the model with the bottom wall of the tunnel section. Pressure distribution measurements on the top and bottom walls of the wind tunnel matched simulation results well. The shock structure in the test section was visualized using the schlieren technique, revealing that the measured angle of the main shock generated at the tip of the rocket matched the simulation data. Finally, the measured forces were compared with simulations for one of the nosecone configurations. Despite very good agreement for pressure distribution on the wind tunnel walls and shock structure, a significant mismatch in the forces measured was nevertheless observed: the simulated CD (0.57) being four times larger than that obtained in measurements (0.138). Further analysis of the test section is required to pinpoint the source of discrepancies and redesign the force measurement system to achieve improved force results.

## Keywords

suborbital rocket, wind tunnel tests, aerospace, drag measurements, supersonic speed.

## 1. INTRODUCTION

The PERUN civil suborbital rocket, currently being designed by the Polish company SpaceForest and co-funded by the Polish National Research and Development Centre [1], aims to reach an altitude of 150 km with a payload of meteorological equipment up to 50 kg in mass, with a maximum speed of over 1500 m/s (Ma=5). This rocket is designed for post-flight element recovery to reduce launch costs. Its inaugural launch is anticipated in 2024.

* Corresponding Author. Email address: fwasilczuk@imp.gda.pl
Received 20.05.2024 • Revised 12.07.2024 • Accepted 12.07.2024

The design of such a rocket is greatly driven by the need to minimize drag and achieve aerodynamic stability. This paper focuses on the former of those two goals, employing numerical simulations to optimize the test section for drag evaluation across various configurations.

The existing literature shows a predominance of experimental approaches, carried out in transonic wind tunnels. Zhang et al. [2] compared numerical results and measurements for supersonic conditions in the range Ma 2.0–4.6 for a two-stage rocket. The model was attached to the tunnel using rear support, installed at the top wall of the test section. Shivananda et al. [3] used experimental measurements to validate their numerical code. They also mounted their model in the wind tunnel using a support attached from the rear. A different approach to obtaining rocket characteristics was employed by Vitale et al. [4], using an aeroballistic facility allowing unrestrained flight.

Since the drag force is one of the key drivers of losses, research aimed at reducing drag for rockets and missiles continues to be of scientific interest. Kim and Al-Obaidi [5] developed a semi-analytical, semi-empirical procedure to calculate the nosecone drag force components – skin friction, base drag, and wave drag. They showed that the base drag is unaffected by the nosecone shape. Moreover, if the nosecone is blunt, the wave drag increases significantly due to the formation of bow shock.

Ukirde and Rathod [6] performed a 2D numerical analysis comparing various nosecone geometries, across sub-, super- and hypersonic regimes. They found that the Ogive-type nosecone resulted in the least drag across regimes. In contrast, Shah et al. [7] established that the Von Karman nosecone is the best across the sub- and supersonic spectrum. The difference may arise from differences in how the turbulence model is defined: Ukirde and Rathod, for instance, used a 2-equation k-ω SST model, while Shah et al. used a 1-equation Spalart Allmaras model.

A wide database of drag characteristics for numerous nosecone shapes was prepared by NASA based on free-flight measurements [8]. The maximum Mach number obtained was 2.0.

Goucem and Khiri [9] performed numerical simulations to assess the forces acting on an air-to-air rocket depending on flight parameters, using ANSYS Fluent. Sahbon et al. [10] performed 3D numerical simulations in ANSYS Fluent for two sounding rocket models with additional steering, to obtain the coefficients for further modeling with lower-fidelity tools.

For suborbital research rockets, such as the PERUN rocket studied in this paper, the characteristics of the rocket during the drop phase are also very important. An experimental study on this fight phase for the ILR-33 AMBER rocket with two parallel stages, including its recovery system, was performed by Marciniak et al. [11]. This test consisted of several drops of the recoverable part from a plane at different heights and with different deployment altitudes of the parachutes used in the recovery system.

Wind-tunnel force measurements similar to those presented in this paper have been performed by Czyż et al. [12] for an unmanned aerial vehicle (UAV). They mounted their model on its back, with support including a 6-axis force sensor. The main goal of their study, to assess stability, made the use of a 6-axis force sensor unavoidable. Their study differed with respect to the model discussed in this paper in terms of the significantly larger size of the UAV model and lower speeds in the wind tunnel.

Another method of mounting the force sensor was employed in the study by Ruchała et al. [13], where a full-scale rocket model was installed in a large (5 m in diameter) test section at the Institute of Aviation in Warsaw. Due to the scale of the model, the force sensor could be installed inside it. In such a configuration the design of the support does not have to include the force sensor. The forces acting on the rocket for varying angles of attack were measured for the velocity of 60 m/s (Ma ~0.17).

This paper consists of 4 sections. After this Introduction, Section 2 presents the design of the test section, including the numerical simulations used for this process and the development of the support shape. Section 3 shows the results of measurements performed in the test section, as well as discussion. The Conclusions section then summarizes the findings of this paper.

## 2. TEST SECTION DESIGN

### 2.1. Wind tunnel

The wind tunnel at the Institute of Fluid-Flow Machinery, Polish Academy of Sciences (IMP PAN) allows supersonic measurements to be performed in test sections with a maximum cross-section of 350 mm × 100 mm.

At the inlet side of the test section, ambient conditions are present, while on the outlet side very low pressure is achieved using vacuum tanks. The low pressure in the vacuum tanks is obtained using pumps, but their power is insufficient to provide continuous operation. Thus, for consecutive measurements the pressure in the vacuum tank has to be reduced again using pumps. This results in a fixed measurement time dependent on the mass flow in the test section.

The wind tunnel allows for the installation of converging/diverging (CD) nozzles to achieve the region with supersonic speed, where models can be placed for measurements. Given the available vacuum tank volume and the scale of the model (see Section 2.3), the CD nozzle was designed using the method of characteristics [14].

The flow velocity achieved in the test section corresponds to Ma=2.45. For such Mach number, the static pressure and temperature in the test section were 6 kPa and 130 K, respectively. The maximum measurement time for such a configuration, given the vacuum tank volume, was 10 seconds for an empty test section and 2.5 seconds

with the model installed, due to increased losses. A numerical model replicating the test section was designed, confirming the values obtained with the method of characteristics, and was further used for in designing the model support.

## 2.2. Rocket model

The rocket model used in this study was scaled down to 1:50 of the original size. The initial length of the model rocket was 200 mm, with a body tube diameter of 10 mm. After initial simulations the model was shortened to 180 mm (while maintaining the same diameter), due to reflected shock interaction (described in depth in Section 2.4). The model also had 4 fins with a span of 6.5 mm, a root chord length of 19 mm, a tip chord length of 8 mm, and a thickness of 0.2 mm. Three models were built with different nose configurations. The nosecone geometry is confidential, but it can be revealed that they were of the Von Karman and Ogive types with a length-to-diameter ratio ($l/d$) of 3.1.

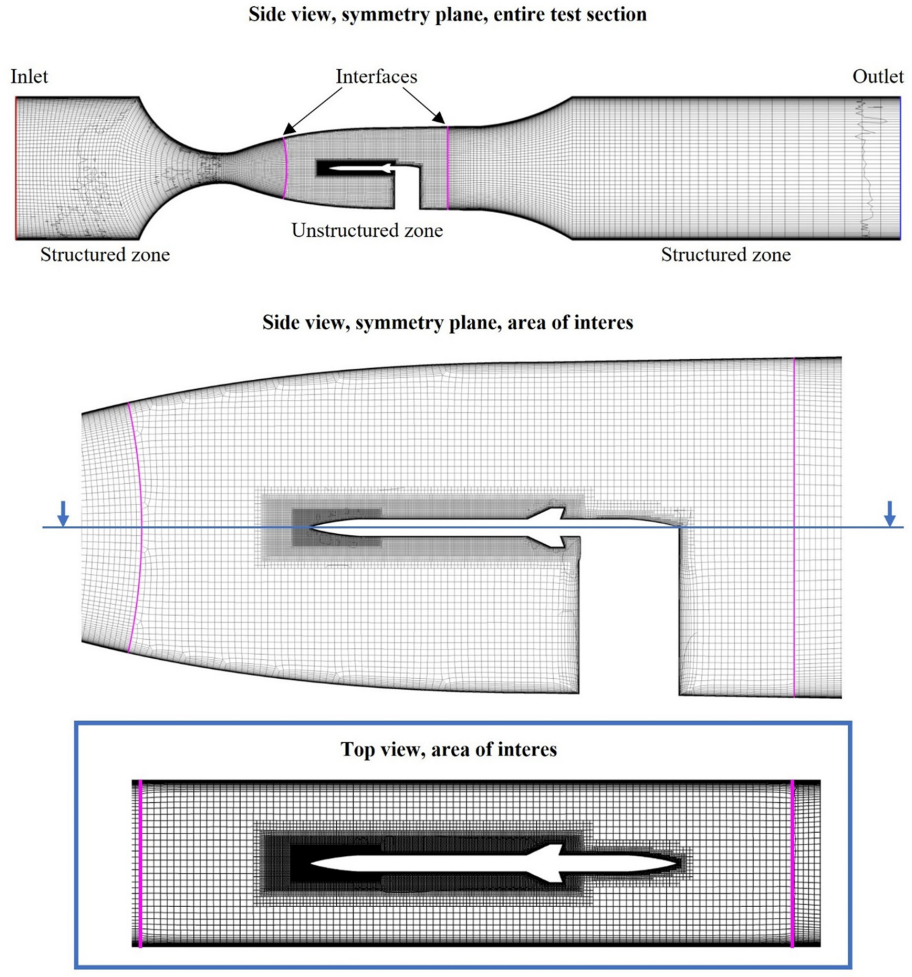


**Fig. 1.** Grid used for numerical simulations. The boundary conditions are presented.

### 2.3. Numerical mode description

The design of the test section was aided by numerical simulations, described in this section.

The simulations were carried out using the finite volume solver Numeca/Fine Open. The method is based on governing equations derived from the principles of mass (Eqn. 1), momentum (Eqn. 2), and energy conservation (Eqn. 3), all shown here after Favre averaging:

$$\frac{\partial \bar{\rho}}{\partial t} + \nabla \bar{\rho} \tilde{U} = 0 \tag{1}$$

$$\frac{\partial \bar{\rho} \tilde{U}}{\partial t} + \nabla \left( \rho \tilde{U} \tilde{U} \right) = -\nabla \bar{p} + \nabla \left( \mu \nabla \tilde{U} \right) - \nabla \overline{\bar{\rho} u' u'} \tag{2}$$

$$\frac{\partial \bar{\rho} \tilde{e}}{\partial t} + \nabla \left( \bar{\rho} \tilde{U} \tilde{e} \right) = \nabla \alpha \nabla \tilde{e} - \nabla \left( \overline{\bar{\rho} u' e'} \right) \tag{3}$$

This formulation of the conservation equations introduces the Reynold stress tensor, which is unknown, thus necessitating the use of the Reynolds Averaged Navier-Stokes (RANS) method. In the RANS method, to solve the system of equations, the Reynold stresses are modeled using one of the available turbulence models. The Spalart-Allmaras model [15] was selected in this work due to its known effectiveness in predicting boundary layer development, which is crucial for force prediction on a body [16].

The entire test section was recreated using a full 3D model. A hybrid numerical mesh is generated in the computational domain (Fig. 1), which was split into three zones: the part upstream of the rocket body, a middle section including the body, and the downstream part. The inlet cavern, nozzle, and outlet cavern were meshed with block-structured, hexahedral mesh using Numeca/IGG. Hexahedral structured meshes are well-posed for meshing simple geometries using a minimal number of elements, while maintaining good mesh quality. However, creating a structured mesh for more complex geometries is challenging. Therefore, an unstructured hexahedral mesh, created in Numeca/Hexpress, was used in the middle zone where the rocket model was placed. The total mesh consists of 7.5 million hexahedral cells.

Since the three zones are meshed with different methods, a non-conformal connection is used at the interface. Despite unavoidable differences between the elements on both sides of the interface, the mesh in both neighboring zones was generated such that their sizes were very similar on both sides (Fig. 1). This similarity makes the interpolation of fluxes at the interface more robust.

Second-order central discretization is used with artificial dissipation for convective terms, and a multigrid method (Full Approximation Storage Approach), including coarse grid initialization with 4 levels, is used to accelerate a solution convergence.

The atmospheric conditions are set at the inlet: total pressure of 100 kPa, total temperature of 297 K, and turbulent viscosity ratio of 1. At the outlet the supersonic condition was set, extrapolating the necessary values from the interior. The medium was set as an ideal gas, with viscosity specification according to Sutherland's law [17].

### 2.4. Numerical mode description

The requirements for the force sensor were quite stringent. It needed to measure low-value forces with low error and withstand high model vibration, necessitating durability. This meant that the forces in the direction normal to the flow could be significantly larger before and after the measurements than those predicted by numerical simulations for Ma=2.45. Force sensors typically have a maximum allowable force, and exceeding this can cause damage. Ideally, the sensor would measure forces and moments in all three axes. It was also crucial that the sensor did not interfere with the flow when coupled with the rocket and the support.

Market research revealed that available force sensors could not meet all these expectations, so some trade-offs were necessary. Two possible approaches were considered:

1) a three-axis force sensor mounted in the test-section floor, measuring forces acting on the rocket and the support.
2) a one-axis force sensor mounted between the rocket model and the support.

The dimensions of the one-axis sensor were ideal for the rocket model – its diameter is equal to the diameter of the model body tube, allowing for easy incorporation within the support. Such a sensor is less prone to failure if the values of normal forces are significant. The obvious drawback of such a configuration is the measurement of only one component of force.

There are no 3-axis force sensors available in the market that are small enough to fit between the rocket model and the support. Thus, mounting the sensor on the floor of the test section, at the base of the support, was considered. This would allow measurement of all three forces and moments. However, this setup would include the support in the force measurements, complicating the detection of small differences between the tested configurations. On the other hand, the measurements could be used for numerical model validation, allowing the various configurations to be tested there. Another issue is that this sensor has low maximum allowable forces (especially in the direction perpendicular to the flow), so it would be very susceptible to failure.

After weighing the advantages and disadvantages , the one-axis sensor was selected. It provides robust measurements of the most critical characteristic – axial force. The selected sensor was the XFTC300-10:

- Measurement range: 0–10 N
- Accuracy: ± 0.05 N
- Sampling frequency: 1000 Hz

The selection of the sensor facilitated the design of the support structure. The most important criterion was the size of the support. If the size (width) is too large the flow is choked and the required conditions in the test section are not achieved. Additionally, the support had to incorporate the wiring needed for the sensor.

The first design of the support (Fig. 2) was prepared and tested using the numerical model of the test section. The width of the support was 10 mm (equal to the model diameter), allowing for a relatively straightforward connection of the necessary wiring. Notably, this width equals 10% of the wind tunnel width in the test section.

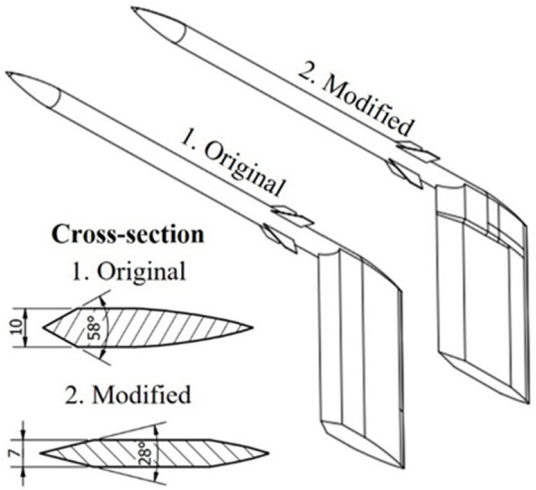


**Fig. 2.** The sketch of the original and modified support, including the cross-section.

Numerical simulations revealed that the initial support design introduced a high blockage, preventing the required Mach number from being reached (Fig. 3). To address this, a new support design with a lower width (7 mm) and modified geometry of the leading edge was proposed. The leading edge angle was adjusted to generate more oblique shock waves. Simulations showed that the new design reduced blockage, enabling the test section to achieve the desired Ma=2.45. The original width was preserved at the top of the support to accommodate the sensor and wiring (Fig. 2).

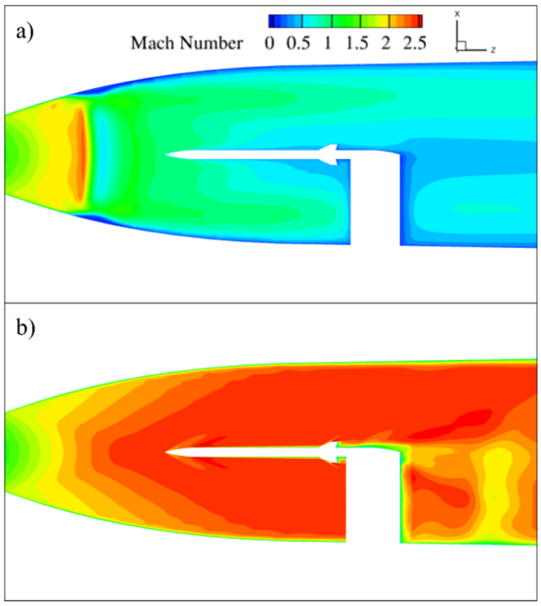


**Fig. 3.** Mach contour plot for configurations with original support (a) and thin support (b) – side view.

The improved support, located within the supersonic region, generates a shock structure. Although the shock is not directly visible in Fig. 3b, as it is located outside of the central plane, it is shown on Fig. 4, where the Mach number contour at half of the support span is presented. Several interesting features, less critical for drag measurement but still noteworthy, can be observed. Firstly, boundary layer separation is present where the oblique shock interacts with the boundary later – happening on both sides of the tunnel, each time the shock interacts with the boundary later. Secondly, higher-velocity zones are created where the shocks reflected from both walls interact with each other in the middle of the tunnel.

However, a low-velocity region downstream of the support is noticeable, where those shockwaves interact after reflection from the wind tunnel sidewalls. Such interaction creates a three-dimensional flow structure downstream of the support but does not create instabilities or unsteady effects on the model located upstream.

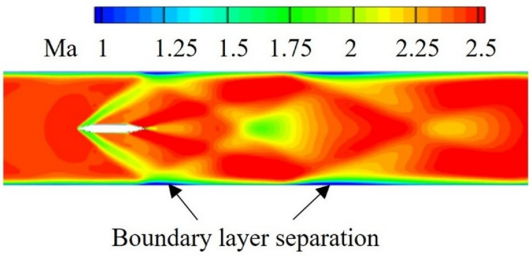


**Fig. 4.** Mach number contour downstream of the support. Cross-section at half of the support span.

Initial simulations allowed for analysis of the shock wave structure in the test section using the density gradient magnitude (Fig. 5). The scale range was selected to visualize the shock structure near the model. Noticeably, the shock generated at the nose of the model reflects from the side walls and impacts the model near the fins.

Such a situation is undesirable, as the shock can significantly impact the flow in that region, interfering with the pressure distribution of the model and affecting the measured drag. Given that the main goal of the study was to compare the nose geometry, the mitigation strategy chosen was to slightly reduce the length of the body tube by 20 mm. This changes the scale of the model, which is no longer consistent with 1:50 in all directions. The nosecone, fins, and diameter are still on a 1:50 scale, while the length of the body tube is not. This modification moves the shock wave reflection downstream, allowing the reflected shock to pass by the model.

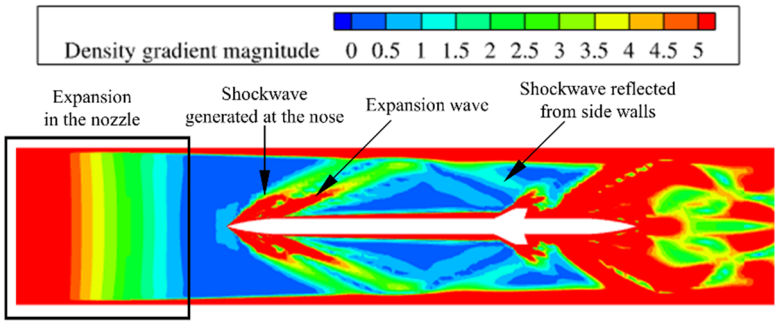


**Fig. 5.** Density gradient magnitude for the model with original length – top view.

## 3. MEASUREMENT RESULTS

### 3.1. Wall presure

First, the pressure distribution at the top and bottom walls of the tunnel were compared for simulations and measurements (Fig. 6). The comparison shows very good agreement, with a decrease in wall pressure observed up to 400 mm from the throat.

On the bottom wall, the presence of the support is visible, with an increase of pressure in the wake downstream of the support. This effect is seen in both measurements and simulations. The results from the top wall show a constant pressure zone between 400 and 600 mm from the throat, which indicates that there is a constant velocity zone as well, which was one of the main design criteria for the nozzle.

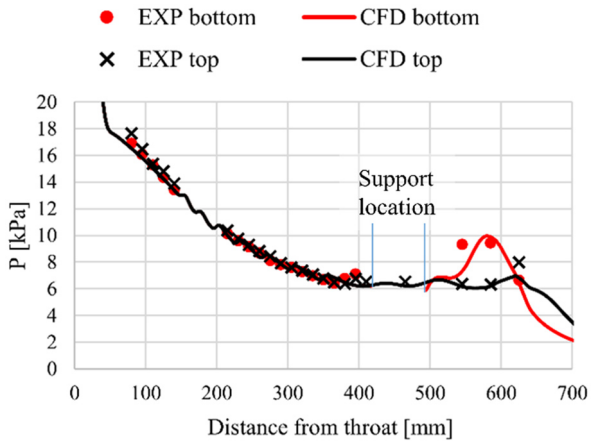


**Fig. 6.** Pressure at top and bottom walls, measurements (EXP) and simulations (CFD).

### 3.2. Shock structure - schlieren visualisation

In addition to force and wall pressure measurements, schlieren visualizations were performed during the experiment (Fig. 7) to analyze the shock structure and compare with numerical simulations to validate the model. The schlieren images show waves in the test section representing compression or expansion. Weak waves can be seen from the left, top, and bottom, generated by the geometry imperfections at the nozzle throat. Slight discontinuities at the top and bottom walls of the nozzle, which result from machining and cannot be detected visually or tactilely, caused two pairs of weak waves seen in Fig. 7.

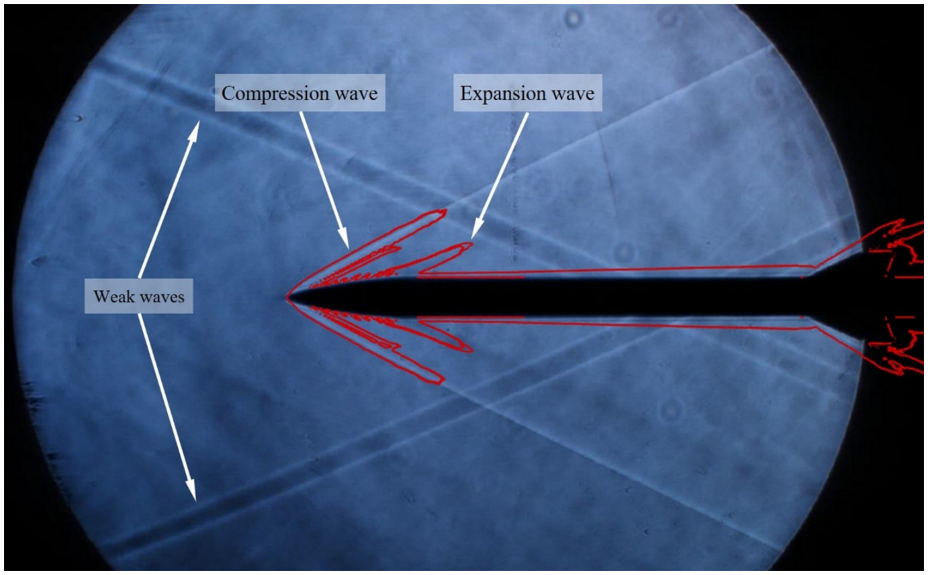


**Fig. 7.** Schlieren visualization for configuration "Nose 2". Red lines are the iso-surface of the density gradient magnitude of 5 kg/m4.

The oblique shock wave generated at the nose of the rocket model was compared to simulation results by plotting an iso-surface of the density gradient magnitude on top of the schlieren picture. This comparison shows that the shock angle predicted by the numerical model is consistent with measurements. The shock wave in the numerical simulations disappears after a short distance from the nose, due to a lower density gradient in this zone due to decreasing grid resolution away from the model rocket. However, the reduced mesh resolution does not affect the prediction of forces on the body. Moreover, the reflected shock from wind tunnel walls does not interact with the model, which was achieved by adjusting its length.

Additionally, the expansion wave can be seen in the schlieren as a slightly darker region, its location conforming with the location of the expansion wave from numerical simulations.

### 3.3. Force measurements

Force measurements were performed for three rocket models with varying nosecones, as described in Section 2.3. Ten consecutive measurement runs were performed for each configuration. Each measurement run consisted of a speed-up phase, where the flow was accelerated and stabilized, and after achieving the required Mach number, force measurements taken for 2.5 seconds, followed by a gradual velocity decrease due to pressure increase in vacuum tanks downstream of the test section.

During the speed-up phase, model vibration occurred due to the flow separation in subsonic and transonic conditions. However, after achieving the required flow conditions and Mach number, the vibrations decreased and the force stabilized at a certain level. Finally, the instantaneous force measurements for various nose configurations were time-averaged and compared with numerical simulations. The unsteady effects caused discrepancies between the consecutive runs, for which a standard deviation of up to 3.4% was recorded.

The force measurements are presented using non-dimensional drag coefficient $C_D$ (Eqn. 4). The reference area assumed for calculation was the frontal area of the rocket model (including fins, but not the support).

$$C_D = \frac{2 \cdot F}{\rho \cdot A \cdot v^2} \tag{4}$$

The drag coefficient CD shown in Fig. 8 presents the mean value from 10 measurements. An error bar denotes the highest and lowest value obtained for each case. In the case of the investigated Mach number, the configuration with the “Nose 2” cone shape proved to be the most effective, with drag 35% lower than the “Nose 1” configuration and 15% lower than the “Nose 3” configuration.

Numerical simulations are presented for one of the configurations – “Nose 2”. The drag coefficient $C_D$ obtained from simulations was significantly larger than the

measurement – $C_D$=0.568. The sizeable discrepancy merits further investigation, especially considering the good agreement between predicted and measured pressure distribution and visualized shock wave structure.

Since there was a significant discrepancy between measured and calculated results, an empirical formula was used to calculate the drag coefficient of a cone with the same angle as the nosecone used. While the actual shape of the nosecone is more complex than a simple cone, the result provides a point of comparison indicating which result is closer to the truth. The formula used was [18]:

$$C_D = \left(0.083 + \frac{0.096}{Ma^2}\right)\left(\frac{\sigma}{10}\right)^{1.69} \tag{5}$$

where: Ma is the Mach number and $\sigma$ is the cone angle in degrees. The $\sigma$ angle was calculated from the nosecone length ($l$) and diameter ($d$) as follows:

$$\sigma = \tan^{-1}\left(\frac{d}{l}\right) \tag{6}$$

The $C_D$ resulting from the empirical formula, accounting only for the pressure drag, was equal to 0.26. This is more consistent with simulation results, where the $C_D$ (from pressure drag and friction drag) obtained was equal to 0.568.

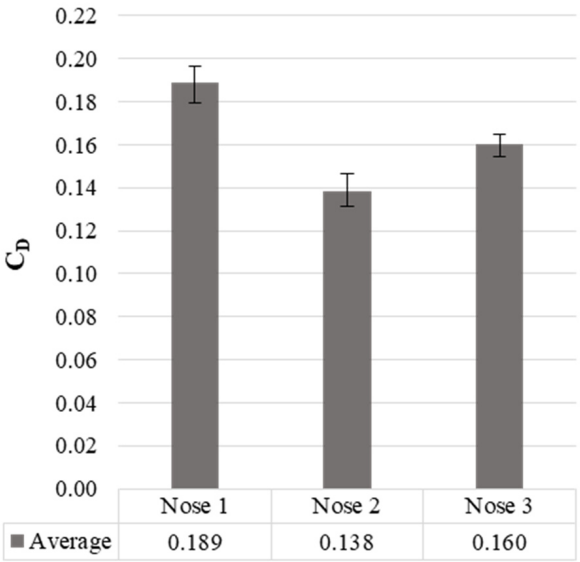


**Fig. 8.** Drag coefficient for three nose configurations.

During the measurements, it was noticed that the model axis deflects slightly upwards when the flow is present. This may cause the one-axis sensor to pick up only a part of the axial force acting on the model. The preferred mitigation strategy

is to repeat the measurement using a sensor that records forces in all directions. As described in section 2.4, the selection of the force sensor was an inherent part of the support design, so it is not possible to change the sensor type and repeat the measurements without significant support redesign.

Based on the numerical simulation results, the contribution of the rocket sectors on the drag can be evaluated. It was found that 65% of the drag is generated by the nosecone, 23% by the body tube, and 12% by the fins. This shows that the nosecone is the dominating source of drag, and it is essential to use optimal geometry to reduce it. Moreover, drag is very sensitive to the nose geometry, and one of the reasons for differences in drag prediction by numerical simulations could be small deviations between the CAD and manufactured models.

## 4. CONCLUSIONS

The paper presents the design methodology for a test section used to investigate the impact of rocket nose configurations on drag. The design was aided with RANS numerical simulations performed in Numeca/FineOpen. The successful nozzle design was confirmed by numerical simulations and pressure measurements. Additionally, the support for the model, which incorporated a one-axis force sensor, was designed and installed in the test section. Preliminary simulations showed that the support introduces a large blockage in the test section, which makes it impossible to achieve the required Mach number. A new, modified support with lower thickness and modified leading edge proved effective.

The pressure measurements at the top and bottom walls of the tunnel showed very good agreement with the simulation results. The shock structure was compared using schlieren images and the density gradient magnitude obtained from simulations, again showing very good agreement in the region with a fine grid.

Finally, the drag coefficient obtained for three nose configurations was investigated. Geometry “Nose 2” showed the lowest drag, 35% lower than “Nose 1” and 15% lower than “Nose 3”. However, the comparison of drag measured for the “Nose 2” configuration with numerical simulation results showed a significant mismatch. Given the very good agreement of other comparisons, it is evident that the force measurement setup should be reconsidered and the details of the manufactured model checked against the CAD model. It is possible that due to some misalignment of the model during the run, the one-axis sensor measures only a part of the drag force even if the misalignment is minimal.

## ABBREVIATIONS

2D – 2 dimensional
3D – 3 dimensional
A – frontal area [$m^2$]
CAD – computer-aided design
CD – converging-diverging
$C_D$ – drag coefficient [-]
CFD – denotes the results obtained using computational fluid dynamics
$d$ – nosecone diameter [m]
EXP – denotes experimental results
F – axial force acting on the rocket model [N]
IMP PAN – Institute of Fluid Flow Machinery, Polish Academy of Sciences
$l$ – nosecone length [m]
Ma – Mach number [-]
P – static pressure [Pa]
RANS – Reynolds Averaged Navier Stokes
UAV – unmanned aerial vehicle
$v$ – velocity [m/s]
$\rho$ – density [$kg/m^3$]
$\sigma$ – cone angle [$^0$]

## REFERENCES


[1] Magiera R, et al, A combustion stabilisation method in a nitrous oxide based hybrid rocket engine. 24th ESA Symposium on European Rocket & Balloon Programmes and related research, 2019 Jun 1–5; Essen, Germany.

[2] Zhang WD, Wang YB, Liu Y, Aerodynamic study of theater ballistic missile target, *Aerospace Science and Technology*, 2013;24(1):221–5. https://doi.org/10.1016/j.ast.2011.11.010.

[3] Shivananda T, McKeel S, Salita M, & Zabrensky E. Space launch vehicle aerodynamics – Comparison of engineering and CFD predictions with wind tunnel data. 39th Aerospace Sciences Meeting and Exhibit.; 2001 Jan 8–11; Reno, NV. https://doi.org/10.2514/6.2001-258.

[4] Vitale R, Abate G, Winchenbach G, & Riner W. Aerodynamic test and analysis of a missile configuration with curvedfins. AIAA 1992-4495 Astrodynamics Conference; 1992 Aug 10–12; Hiton Head, SC. https://doi.org/10.2514/6.1992-4495.

[5] Kim BK, Al-Obaidi ASM. Investigation of the effect of nose shape and geometry at supersonic speeds for missile performance optimization, *J. Phys.: Conf. Ser*. 2023; 2523: 012010, https://doi.org/10.1088/1742-6596/2523/1/012010.

[6] Ukirde K, Rathod S. Aerodynamic analysis of various nose cone geometries for rocket launch vehicle at different Mach regimes. *AIP Conf. Proc*. 11 December 2023; 2855(1):020004.

[7] Shah S, Tanwani N, Singh SK, Makwana MM. Drag Analysis for Sounding Rocket Nose Cone. *International Research Journal of Engineering and Technology*. 2020;7(7).

[8] Seiff A, Sandahl CA. Aerodynamic Characteristics of Bodies at Supersonic Speeds: A Collection of Three Papers, NACA Conference on Aerodynamic Design Problems of Supersonic Guided Missiles (1951). *Review of Aerospace Engineering*. 2023;16(5).

[9] Goucem M, Khiri R. Optimizing Supersonic Rocket Efficiency: A Numerical Analysis of Aerodynamic Characteristics and Angle of Canard Deflection. *International Review of Aerospace Engineering*. 2023;16(5), https://doi.org/10.1108/IRA-2023-0050.

[10] Sahbon N, Murpani S, Michałów M, Miedziński D, Sochacki M. A CFD Study of the Aerodynamic Characteristics of Twardowsky and FOK Rockets. *Transactions on Aerospace Research*. 2022(1):35–58. https://doi.org/10.2478/tar-2022-0003

[11] Marciniak BA, Cieśliński D, Matyszewski J. Verifying the ILR-33 AMBER Rocket Recovery System by Means of a Drop Test Campaign. *International Review of Aerospace Engineering*. 2023;16(1)

[12] Czyż Z., Karpiński P., Skiba K., Wendeker M. Measurements of Aerodynamic Performance of the Fuselage of a Hybrid Multi-Rotor Aircraft with Autorotation Capability. *International Review of Aerospace Engineering*. 2022;15(1).

[13] Ruchała P, Placek R, Stryczniewicz W, Matyszewski J, Cieśliński D, Bartkowiak B. Wind tunnel tests of influence of boosters and fins on aerodynamic characteristics of the experimental rocket platform. *Transactions on Aerospace Research*. 2017(4):82–102. https://doi.org/10.2478/tar-2017-0030.

[14] Angelino G. Approximate method for plug nozzle design. *AIAA Journal*. 1964, 2(10):1834–1835. https://doi.org/10.2514/3.2682.

[15] Spalart P, Allmaras S. A one-equation turbulence model for aerodynamic flows, AIAA 1992-439. 30th Aerospace Sciences Meeting and Exhibit. 1992 Jan 6–9; Reno, NV. https://doi.org/10.2514/6.1992-439.

[16] Szulc O, Doerffer P, Flaszynski P, Braza M., Moving wall effect on normal shock wave–turbulent boundary layer interaction on an airfoil. *International Journal of Numerical Methods for Heat & Fluid Flow*. 2023. https://doi.org/10.1108/HFF-06-2023-0338.

[17] Sutherland, W. LII. The viscosity of gases and molecular force. *The London, Edinburgh, and Dublin Philosophical Magazine and Journal of Science*. 1893; 36(223),507–531. https://doi.org/10.1080/14786449308620508.

[18] Chin SS. Missile Configuration Design, McGraw-Hill, New York, 1961.